JACS
JOURNAL OF THE AMERICAN CHEMICAL SOCIETY

ARTICLE

pubs.acs.org/JACS

Mn(I) in an Extended Oxide: The Synthesis and Characterization of $La_{1-x}Ca_xMnO_{2+\delta}$ ($0.6 \leq x \leq 1$)

Edward Dixon,[†] Joke Hadermann,[‡] Silvia Ramos,[§] Andrew L. Goodwin,[†] and Michael A. Hayward*[,†]

[†]Department of Chemistry, University of Oxford, Inorganic Chemistry Laboratory, South Parks Road, Oxford, OX1 3QR, United Kingdom

[‡]EMAT, University of Antwerp, Groenenborgerlaan 171, B-2020 Antwerp, Belgium

[§]Diamond Light Source Ltd., Harwell Science and Innovation Campus, Didcot OX11 0DE, United Kingdom

Supporting Information

ABSTRACT: Reduction of $La_{1-x}Ca_xMnO_3$ ($0.6 \leq x \leq 1$) perovskite phases with sodium hydride yields materials of composition $La_{1-x}Ca_xMnO_{2+\delta}$. The calcium-rich phases ($x = 0.9, 1$) adopt $(La_{0.9}Ca_{0.1})_{0.5}Mn_{0.5}O$ disordered rocksalt structures. However local structure analysis using reverse Monte Carlo refinement of models against pair distribution functions obtained from neutron total scattering data reveals lanthanum-rich $La_{1-x}Ca_xMnO_{2+\delta}$ ($x = 0.6, 0.67, 0.7$) phases adopt disordered structures consisting of an intergrowth of sheets of MnO_6 octahedra and sheets of MnO_4 tetrahedra. X-ray absorption data confirm the presence of Mn(I) centers in $La_{1-x}Ca_xMnO_{2+\delta}$ phases with $x < 1$. Low-temperature neutron diffraction data reveal $La_{1-x}Ca_xMnO_{2+\delta}$ ($x = 0.6, 0.67, 0.7$) phases become antiferromagnetically ordered at low temperature.

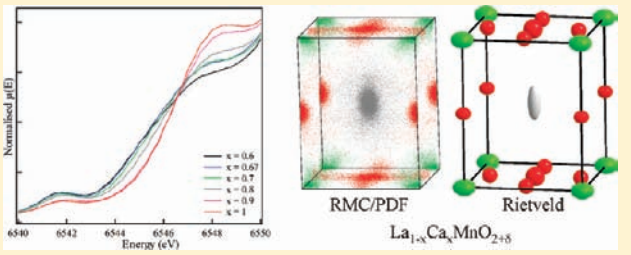

INTRODUCTION

Complex transition metal oxides are of wide and enduring interest because they exhibit a diverse array of physical behavior including high-temperature superconductivity,[1] magnetoresistance,[2] ferroelectricity[3] and an extensive range of other coupled magnetic and electronic responses.[4] As a result transition metal oxide phases are found in applications as diverse as lithium ion battery electrodes,[5] microwave dielectrics for mobile communications[6] and numerous catalytic systems.[7]

The diverse and complex electronic behavior exhibited by transition metal oxides can be attributed to the presence of partially occupied d-orbitals/states which interact through the extended metal−oxygen lattice[8] resulting in strongly correlated electronic states. It therefore follows that an effective strategy for the discovery of new materials which exhibit novel physical behavior, is the preparation of metal oxide phases which contain novel extended metal−oxygen networks of electronically coupled transition metal centers.

The high-temperature solid-state reactions conventionally used to make complex oxide phases are limited in their ability to prepare novel materials as they are almost inevitably performed under conditions which 'select' product phases on the basis of thermodynamic stability. As a result, for a given chemical composition, only the phase or mixture of phases with the most stable atomic configuration can be prepared, precluding the formation of metastable materials.

In contrast, low-temperature 'soft' chemical syntheses can be utilized to exert kinetic control over product selection, greatly extending the range of materials that can be formed.[9−11] Low-temperature reductive oxygen deintercalation is a particularly useful 'soft' chemical method for the preparation of novel transition metal oxide phases. By exploiting the observation that anions are significantly more mobile than cations within extended metal-oxide frameworks, low-temperature reduction reactions can be performed which allow the removal of oxygen from complex oxide phases, with retention of the overall cation configuration. These structure-conserving topotactic reduction reactions allow the preparation of complex metal oxide phases which contain transition metal centers in unusual oxidation states and coordination geometries. Thus, for example, by utilizing binary metal hydrides as low-temperature reducing agents it is possible to prepare metastable phases containing square-planar Ni(I),[12,13] Co(I)[14] or Fe(II)[15,16] centers.

Recently, we have been studying the low-temperature reduction chemistry of $La_{1-x}A_xMnO_3$ (A = Ba, Sr, Ca) perovskite phases in order to prepare mixed valent Mn(II/III) materials.[17−19] Here we report the preparation of phases of composition $La_{1-x}Ca_xMnO_{2+\delta}$ ($0.6 \leq x \leq 1$) which contain significant concentrations of monovalent manganese centers. To the best of our knowledge this is the first observation of Mn(I) centers in an extended oxide phase.

EXPERIMENTAL SECTION

Preparation of $La_{1-x}Ca_xMnO_3$ Phases. Samples of $La_{1-x}Ca_xMnO_3$ ($x = 0.6, 0.67, 0.7, 0.8, 0.9$ and 1) were prepared using a standard ceramic

Received: August 12, 2011
Published: October 14, 2011

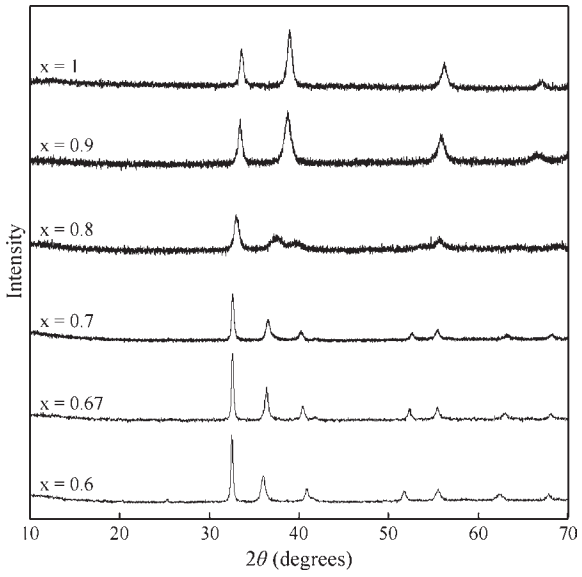

Figure 1. X-ray powder diffraction data collected from reduced phases of composition $La_{1-x}Ca_xMnO_{2+\delta}$.

route. Appropriate stoichiometric ratios of La_2O_3 (99.999%, dried at 900 °C), $CaCO_3$ (99.999%) and MnO_2 (99.999%) were thoroughly mixed in an agate pestle and mortar and then heated at 1000 °C in air to decompose the carbonate. The resulting black powders were then reground, pressed into 13 mm pellets with a force of 5 tonnes and heated in air at either 1350 °C ($0.6 \leq x \leq 0.9$) or 1150 °C ($x = 1$) for 3 periods of 48 h with intermittent regrinding. After the final heating cycle, the samples were cooled to room temperature at 1 °C min^{-1} to ensure full oxygen stoichiometry was achieved. X-ray powder diffraction data collected from these materials were consistent with single phase samples with lattice parameters in agreement with those previously reported.[20,21]

Reduction of $La_{1-x}Ca_xMnO_3$ phases. Reduction of the $La_{1-x}Ca_xMnO_3$ phases was performed using NaH (>95%) as a solid-state reducing agent.[12] Approximately 4 g of the required $La_{1-x}Ca_xMnO_3$ phase was mixed with two mole equivalents of NaH in an argon-filled glovebox (O_2 and H_2O < 1 ppm). The resulting mixtures were then sealed under vacuum in Pyrex tubes and heated for 24 h at 180 °C and then for a further 24 h at 210 °C. The samples were then reground and resealed before being heated for 3 further periods of 48 h at 210 °C. Finally samples were washed with 4 × 100 mL of methanol under a nitrogen atmosphere to remove sodium-containing phases (NaOH and NaH) before being dried under vacuum.

Characterization. X-ray powder diffraction data were collected using a PANalytical X'Pert diffractometer incorporating an X'celerator position sensitive detector (monochromatic Cu $K_{\alpha 1}$ radiation). Neutron powder diffraction data were collected from samples, contained within vanadium cans sealed under an argon atmosphere with an indium washer, using either the POLARIS diffractometer (ISIS neutron source, U.K.; $La_{1-x}Ca_xMnO_2$, x = 0.6, 0.67 and 0.7) or the D2b diffractometer (ILL neutron source, Grenoble; $La_{1-x}Ca_xMnO_2$, $x = 0.8$ and 0.9) at a wavelength of λ = 1.59 Å. Rietveld profile refinement was performed using the GSAS suite of programs.[22] Electron diffraction data were collected from finely ground samples supported on holey carbon grids (deposited from suspension in ethanol) using a Philips CM20 microscope.

X-ray absorption data were collected at the beamline B18 (Diamond Light Source, UK) using the Pt branch and a double crystal monochromator with Si 111 crystals. Harmonic rejection mirrors were also used in order to eliminate the harmonic content in the beam for the Mn K-edge measurements. The samples were optimized for measurement in fluorescence mode and data were collected using a 9-element Ge detector.

Neutron total scattering data were collected using the POLARIS diffractometer (ISIS neutron source, U.K.; $La_{1-x}Ca_xMnO_2$, $x = 0.6$, 0.67 and 0.7). Normalized neutron total scattering functions $F(Q)$ ($1.5 \leq Q \leq 40$ Å^{-1}) were obtained by merging data from both 90° and backscattering (130−160°) detector banks and applying a standard series of smooth data corrections to account for background scattering and sample absorption effects.[23] The neutron pair distribution functions $G(r)$ obtained as reverse Fourier transforms of these data formed the basis of reverse Monte Carlo (RMC) refinements using the program RMCProfile.[24]

Table 1. Lattice Parameters Determined from X-ray Powder Diffraction Data Collected from $La_{1-x}Ca_xMnO_{3-y}$ ($0.6 \leq x \leq 1$) Phases

$La_{1-x}Ca_xMnO_{3-y}$	a (Å)	c (Å)	c/a	V (Å^3)
0.6	3.539(1)	4.428(1)	1.251	55.47(4)
0.67	3.508(1)	4.455(1)	1.269	54.85(2)
0.7	3.480(1)	4.489(1)	1.289	54.37(3)
0.8	3.382(2)	4.602(3)	1.360	52.65(9)
0.9	4.661(1)			101.30(7)
1	4.637(1)			99.70(5)

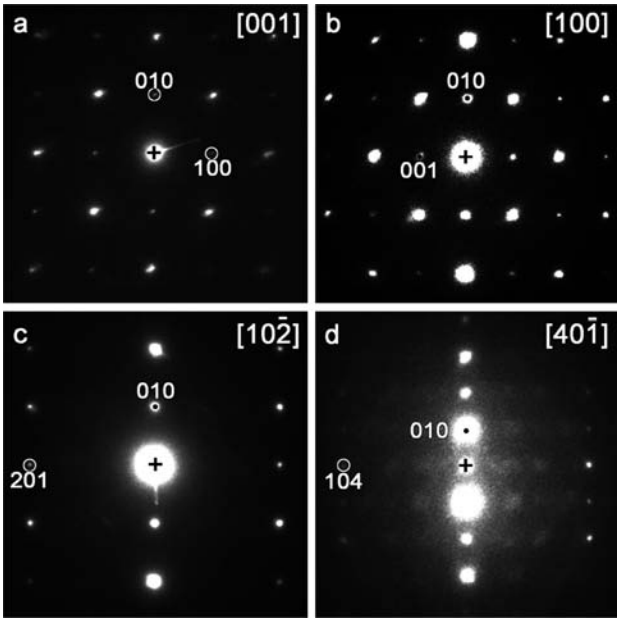

Figure 2. Electron diffraction data collected from the [001], [100], [−102], and [−401] zones of $La_{0.4}Ca_{0.6}MnO_2$. Data from the [−401] zone show extensive diffuse scattering consistent with short-range order within the anion lattice.

RESULTS

Structural Characterization. X-ray powder diffraction data, collected from the washed products of the reactions between $La_{1-x}Ca_xMnO_3$ phases and NaH (Figure 1), could be readily indexed using the unit cells listed in Table 1. Data collected from the x = 1 and x = 0.9 samples are consistent with reduced materials adopting rock-salt structures with disordered cation

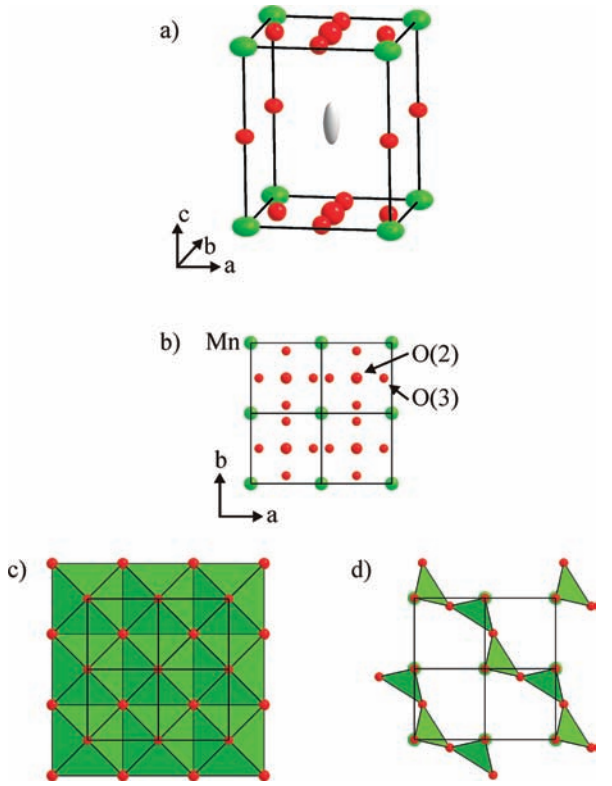

Figure 3. (a) The refined structure of $La_{1-x}Ca_xMnO_2$ (x = 0.6, 0.67, 0.7). (b) Oxygen distribution in the *ab*-plane can be separated into two layers of composition MnO consisting of either (c) edge-sharing MnO_6 octahedra or (d) brownmillerite-like corner-sharing MnO_4 tetrahedra. In all parts of the figure oxide ions are red, manganese ions are green, and La/Ca cations are gray.

lattices, best represented as $(La_{1-x}Ca_x)_{0.5}Mn_{0.5}O$, in agreement with previous studies of the hydrogen reduction of $CaMnO_3$ to '$CaMnO_2$' by Varela et al.[25] Structural models based on cation-disordered rock salt structures gave good statistical fits to the X-ray (x = 1, 0.9) and neutron (x = 0.9) powder diffraction data collected from these reduced samples, confirming this structural assignment as detailed in the Supporting Information.

In contrast to data from the calcium-rich phases, X-ray powder diffraction data collected from reduced phases of composition $La_{1-x}Ca_xMnO_{3-y}$ ($0.6 \leq x \leq 0.7$) could be indexed using primitive tetragonal unit cells, suggesting that the cation lattice of the parent perovskite materials has been retained in these reduced products. In order to confirm the size and symmetry of the unit cells determined for the lanthanum-rich reduced materials, electron diffraction data were collected from $La_{0.4}Ca_{0.6}MnO_{3-y}$, selected as a representative member of the $La_{1-x}Ca_xMnO_{3-y}$ ($0.6 \leq x \leq 0.8$) series. As shown in Figure 2 these data are consistent with the tetragonal unit cells determined from the X-ray diffraction data (Table 1); however, data collected from several zones contain diffuse scattering, indicative of additional short-range order within these reduced phases.

Neutron powder diffraction data collected at room temperature from the $La_{1-x}Ca_xMnO_{3-y}$ ($0.6 \leq x \leq 0.7$) reduced phases could also be readily indexed using the primitive unit cells detailed in Table 1. Good statistical fits to these data could be achieved using structural models with the same cationic arrangement as in the corresponding perovskite starting materials (La/Ca - (1/2, 1/2, 1/2) and Mn - (0, 0, 0)) but with three distinct anion sites: O(1) - (0, 0, 1/2), O(2) - (1/2, 1/2, 0) and O(3) - (x, 1/2, 0) as shown in Figure 3a,b. Observed, calculated, and difference plots from these refinements are shown in Figure 4, with the structural parameters refined for $La_{1-x}Ca_xMnO_{3-y}$ (x = 0.6, 0.67, 0,7) phases shown in Table 2.

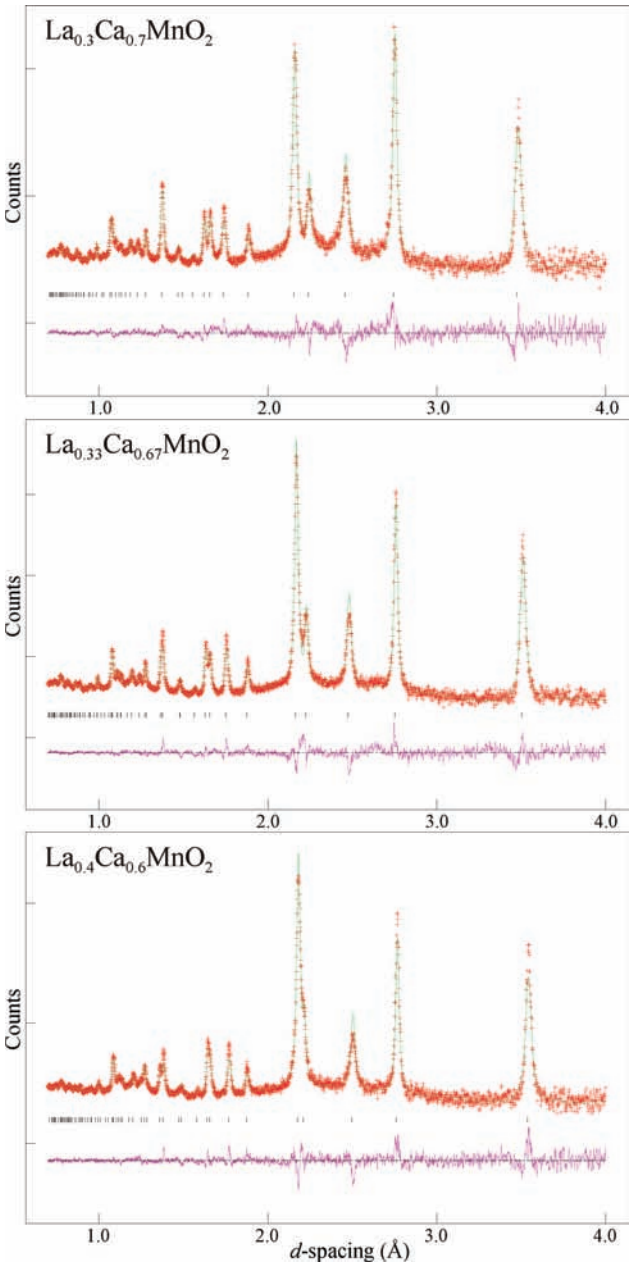

Figure 4. Observed, calculated, and difference plots from the structural refinements of $La_{1-x}Ca_xMnO_{2+\delta}$ phases against neutron powder diffraction data collected at room temperature.

Chemical Characterization. As described above, diffraction data collected from the reduced phases allow the refinement of structural models which are consistent with compositions of $La_{1-x}Ca_xMnO_{2+\delta}$, for all the samples in the range $0.6 < x < 1$. These compositions imply that samples with $x < 1$ contain manganese centers with average oxidation states which are less than Mn+2. The presence of monovalent manganese in an extended oxide is unprecedented, therefore it is clearly important to

Table 2. Structural Parameters Refined for $La_{1-x}Ca_xMnO_{3-y}$ Phases against Room Temperature Neutron Diffraction Data[a]

		x = 0.6	x = 0.67	x = 0.7
La/Ca	fraction	0.4/0.6	0.33/0.67	0.3/0.7
	$U_{11} = U_{22}$	0.016(1)	0.010(1)	0.051(4)
	U_{33}	0.112(1)	0.105(1)	0.119(1)
Mn	$U_{11} = U_{22}$	0.049(1)	0.055(1)	0.055(1)
	U_{33}	0.025(1)	0.033(1)	0.025(1)
O(1)	$U_{11} = U_{22}$	0.022(1)	0.018(1)	0.014(1)
	U_{33}	0.015(1)	0.020(1)	0.012(1)
O(2)	fraction	0.541(4)	0.572(3)	0.662(4)
	U_{iso}	0.035(1)	0.032(1)	0.030(1)
O(3)	x	0.114(1)	0.107(1)	0.123(1)
	fraction	0.115(1)	0.118(1)	0.085(1)
	U_{iso}	0.022(1)	0.019(1)	0.031(2)
refined composition: $La_{1-x}Ca_xMnO_z$		2.001(5)	2.044(5)	2.002(5)
lattice parameters	a (Å)	3.5387(4)	3.5066(2)	3.4782(3)
	c (Å)	4.4247(6)	4.4529(4)	4.4856(4)
χ^2		1.453	1.853	1.677

[a] Space group: $P4/mmm$. Atomic positions: La/Ca: 1*d*, (1/2,1/2,1/2); Mn: 1*a*, (0, 0, 0); O(1): 1*b* (0, 0, 1/2); O(2): 1*c* (1/2,1/2, 0); O(3) 4*n* (x, 1/2, 0).

confirm the stoichiometries obtained from the structural models independently.

The oxygen contents of the two $La_{1-x}Ca_xMnO_{2+\delta}$ samples which adopt disordered rock salt structures (x = 0.9, 1) are clear and unambiguous from the structural refinements. However, strong correlations between displacement parameters and fractional occupancies within the complex structures of the remaining $La_{1-x}Ca_xMnO_{2+\delta}$ phases result in a degree of uncertainty in the stoichiometries determined for these lanthanum-rich samples. Attempts to determine the oxygen stoichiometry of the reduced $La_{1-x}Ca_xMnO_{2+\delta}$ phases gravimetrically were unsuccessful as neither oxidation with oxygen or reduction with hydrogen yielded products of well-defined stoichiometry. In addition dissolution of samples in an acidified solution of KI (iodometry) did not yield any iodine, demonstrating that the $La_{1-x}Ca_xMnO_{2+\delta}$ phases have average manganese oxidation states of Mn+2 or lower, but preventing a more exact characterization.

Therefore, in order to unambiguously determine the oxidation states of the manganese centers present in $La_{1-x}Ca_xMnO_{2+\delta}$ phases, X-ray absorption spectra were collected. The x = 1 sample, $Ca_{0.5}Mn_{0.5}O$, has a well-defined stoichiometry and thus a well-defined manganese oxidation state (Mn+2), and so the Mn K-edge absorption of this phase was used as a standard in the subsequent analysis. XANES data plotted in Figure 5 clearly show that the manganese K-edge absorption moves to lower energy with decreasing x (decreasing calcium content). This is entirely consistent with the expected reduction in manganese oxidation state with decreasing x. Given that the x = 1 sample has a manganese oxidation state of Mn+2, these data clearly and unambiguously demonstrate the presence of monovalent manganese centers in $La_{1-x}Ca_xMnO_{2+\delta}$ phases, and are consistent with oxygen stoichiometries obtained from the structural refinements (Table 2).

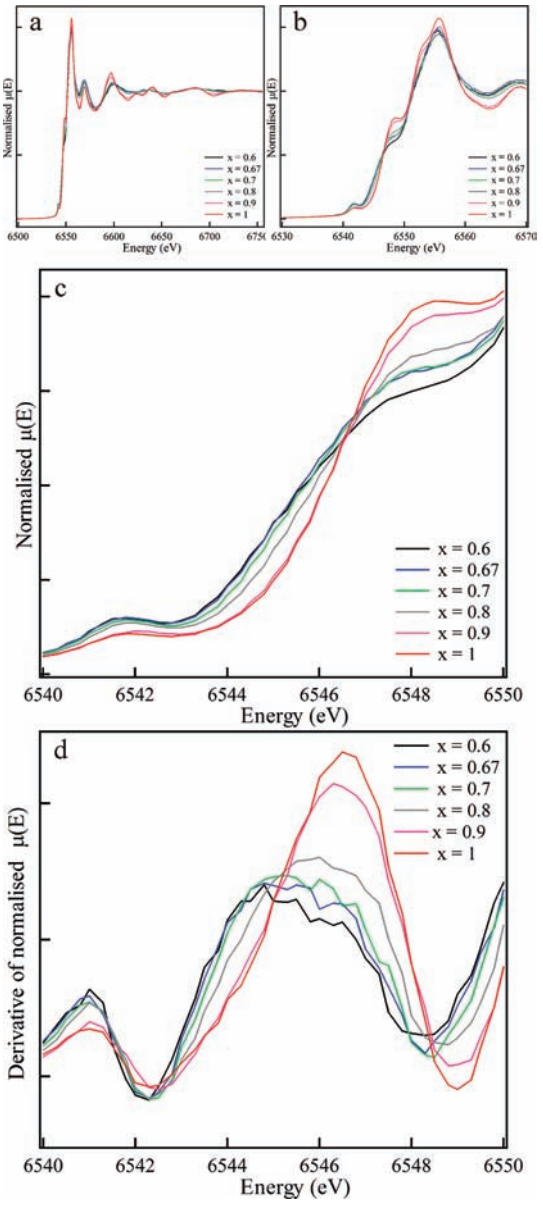

Figure 5. (a, b, c) Normalized X-ray absorption spectra collected from the manganese K-edge of $La_{1-x}Ca_xMnO_{2+\delta}$ phases. (d) The derivative of the normalized absorption spectra, highlighting the shift to lower energy of the edge position with decreasing x.

Local Structure. The positions of the O(2) and O(3) oxygen sites within the structural models refined for the $La_{1-x}Ca_xMnO_{2+\delta}$ (x = 0.6, 0.67, 0.7) phases are too close to each other to be occupied simultaneously (Figure 3b). This indicates that the models refined for the $La_{1-x}Ca_xMnO_{2+\delta}$ (x = 0.6, 0.67, 0.7) phases describe disordered structures which contain a number of distinct local anion arrangements which are superimposed within the model. This disorder exists primarily within the z = 0 planes. The atomic arrangement within these planes can be readily deconvoluted into two separate, chemically reasonable layers, both of composition MnO. Layer type 1 contains the manganese site and the O(2) anion site, and consists of a layer of edge-sharing MnO_6 octahedra as shown in Figure 3c, which we will refer to as an octahedral layer. Layer type 2 contains the manganese site and the O(3) anion site. The disposition of the O(3) anion sites is

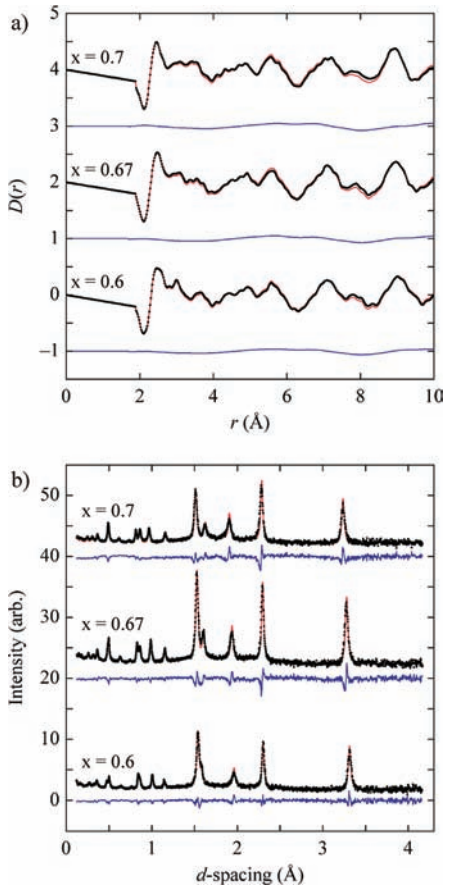

Figure 6. RMC fits to (a) the pair distribution functions and (b) Bragg profiles collected from $La_{1-x}Ca_xMnO_{2+\delta}$ phases.

such that only one site can be occupied in each unit cell, if unphysically short oxygen−oxygen separations are to be avoided. This suggests an anion arrangement as shown in Figure 3d, consisting of chains of corner-sharing MnO_4 tetrahedra (reminiscent of the anion-deficient layers in brownmillerite and related structures)[18] which we will refer to as a tetrahedral layer. We propose that the structures of the $La_{1-x}Ca_xMnO_{2+\delta}$ (x = 0.6, 0.67, 0.7) phases consist of disordered stacked arrays of these two layer types.

In order to confirm and explore the local structures of the $La_{1-x}Ca_xMnO_{2+\delta}$ phases, reverse Monte Carlo (RMC) refinements were performed, guided by the pair distribution functions (PDF) obtained from corrected neutron total scattering data in the range $1.5 < Q/Å^{-1} < 40$. Initial atomic configurations for RMC optimization were created for each composition, on the basis of the disordered stacking of octahedral and tetrahedral layers, within supercells which were 20 × 20 × 26-fold expansions of the corresponding refined crystallographic cells. The initial positions of atoms within octahedral layers were extracted directly from the refined structural models (Table 2). Due to the average tetragonal symmetry observed for the $La_{1-x}Ca_xMnO_{2+\delta}$ phases, four different tetrahedral layer types were created to allow the chains of tetrahedra within these layers to propagate along the [110] or [1−10] directions with either 'left'- or 'right'-handed twists, as described in detail in the Supporting Information. Ensembles were constructed by the disordered stacking of randomly chosen tetrahedral and octahedral layers, to achieve an octahedral:tetrahedral layer ratio which reflected the fractional occupancies of the O(2) and O(3) anion sites refined for each composition ($La_{0.4}Ca_{0.6}MnO_2$ = 14:12; $La_{0.33}Ca_{0.67}MnO_2$ = 15:11; $La_{0.3}Ca_{0.7}MnO_2$ = 17:9). The disordered arrangement of the lanthanum and calcium cations within structures was modeled using 'hybrid' A-cation sites with neutron scattering lengths equal to the weighted average of the A-cations in the empirical composition. Atomic positions corresponding to the refined O(1) anion sites were also added between layers, to retain the overall $La_{1-x}Ca_xMnO_2$ stoichiometries of the models.

Five separate configurations, each with their own random distribution of octahedral and tetrahedral layers, were generated for each $La_{1-x}Ca_xMnO_2$ composition. Two separate RMC optimizations were performed on each configuration. RMC simulations were guided simultaneously by fits to both the PDF and Bragg diffraction data after imposing two key constraints on the refined configurations. (1) The closest approach of atomic pairs was maintained above a minimum value which depended on the identity of the atoms concerned, as described in the Supporting Information. (2) Mn−O bond lengths were constrained to lie in the range 1.7−3 Å to conserve the connectivity of the Mn−O network.

The final atomic configurations generated by the RMC simulations yielded good fits to the appropriate experimental differential correlation functions, and to the corresponding neutron diffraction data sets as shown in Figure 6. There were only minor differences between the atomic configurations generated in each of the 10 RMC simulations for each composition, indicating that the overall result is largely independent of the starting configuration.

As a final check of the quality of the RMC models, inspection of slices though the MnO layers (Figure 7) reveals that the refinement has proceeded without the inclusion of any anomalous regions of 'damage', to produce atomic configurations with chemically reasonable atomic separations. It can also be seen that the overall topologies of the MnO layers are similar to those in the starting configurations, suggesting that segregation into octahedral and tetrahedral layers is a real feature of the structures. The final atomic configuration from the RMC simulation for $La_{0.4}Ca_{0.6}MnO_{2+\delta}$, 'collapsed' into the simple disordered crystallographic unit cell, is shown in Figure 8. Reassuringly, the 'collapsed' structure is very similar to the average structure extracted from Rietveld refinement against bulk diffraction data (Figure 3a). Bond-lengths calculated from the average-structure determinations, ⟨A⟩−⟨B⟩, and RMC optimizations, ⟨A−B⟩, of the $La_{1-x}Ca_xMnO_2$ (0.6, 0.67, 0.7) phases are listed in Table 3.

Magnetic Characterization. Low-temperature neutron powder diffraction data collected from $La_{1-x}Ca_xMnO_{2+\delta}$ (x = 0.6, 0.67, 0.7) samples exhibited additional large d-spacing diffraction peaks, compared to the analogous room temperature data, indicative of long-range magnetic order. The additional reflections could be readily indexed on the basis of $a' = \sqrt{2}a$, $b' = \sqrt{2}b$, $c' = 2c$ expansions of the corresponding crystallographic cells, with intensities best accounted for by simple G-type antiferromagnetically ordered models (Figure 9). Fits of the temperature dependence of the refined ordered moments to an $I = A(1 - (T/T_N))^{\beta}$ power law, using parameters listed in Table 4, yielded antiferromagnetic ordering temperatures of 231, 221, and 214 K for $La_{0.4}Ca_{0.6}MnO_{2+\delta}$, $La_{0.33}Ca_{0.67}MnO_{2+\delta}$, and $La_{0.3}Ca_{0.7}MnO_{2+\delta}$, respectively (Figure 9). Observed, calculated, and difference plots from the nuclear and magnetic fits to neutron powder diffraction data collected from samples at 5 K, are shown in the Supporting Information.

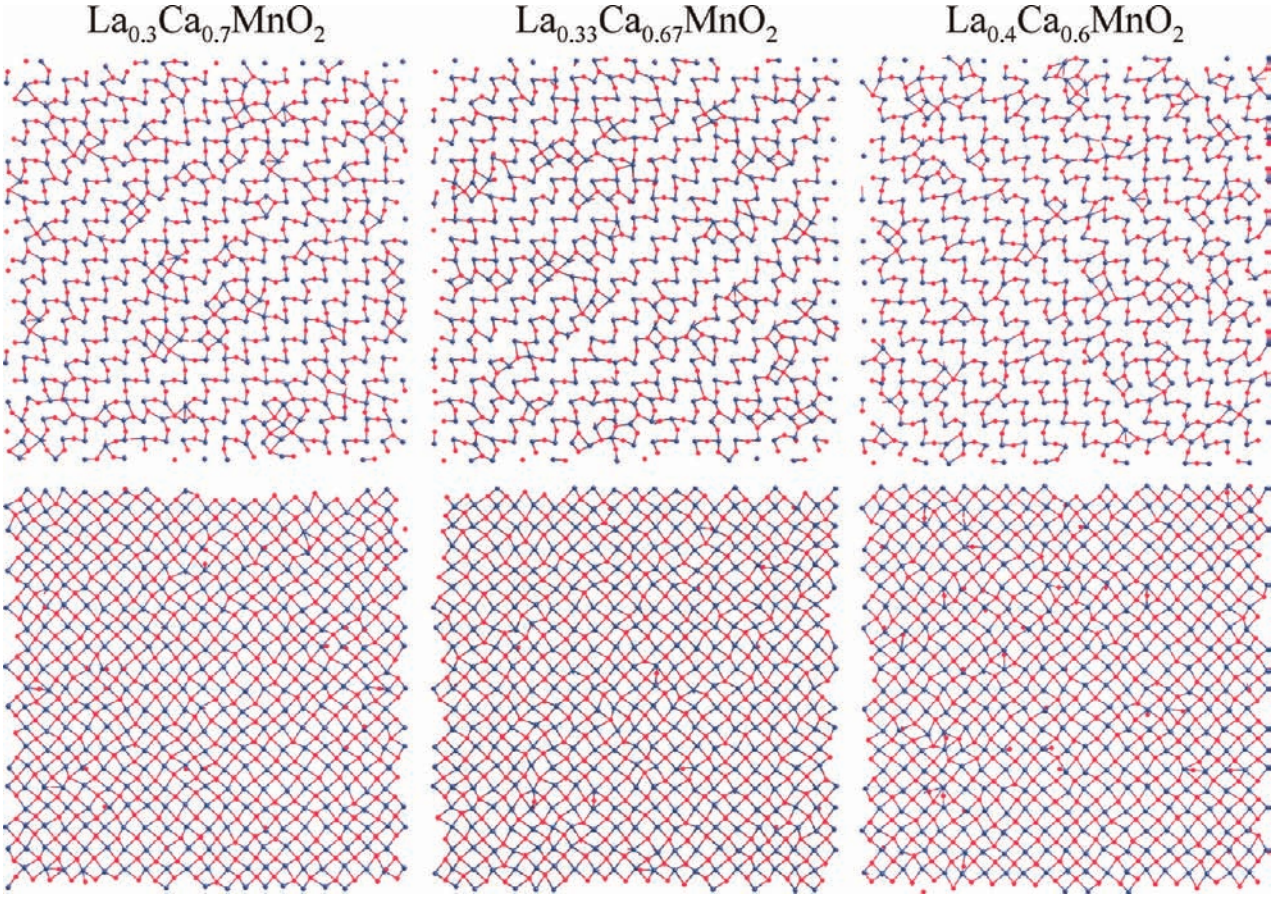

Figure 7. Slices through the tetrahedral (top) and octahedral (bottom) layers of the final RMC atomic configurations of $La_{1-x}Ca_xMnO_{2+\delta}$ phases. Blue spheres represent manganese, red spheres represent oxide ions.

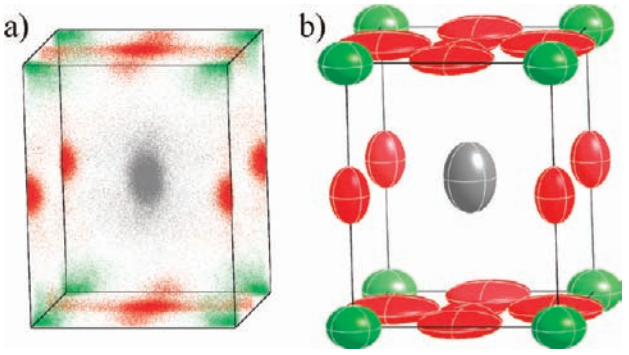

Figure 8. (a) 'Collapsed' structure from RMC simulation of $La_{0.4}Ca_{0.6}MnO_2$. (b) Description of 'collapsed' structure using displacement ellipsoids. In all parts of the figure oxide ions are red, manganese ions are green, and La/Ca cations are gray.

DISCUSSION

Reduction of $La_{1-x}Ca_xMnO_3$ ($0.6 \leq x \leq 1$) perovskite phases with sodium hydride yields materials of composition $La_{1-x}Ca_xMnO_{2+\delta}$ which adopt one of two different crystal structures, depending on the La:Ca ratio. Reduced phases with low lanthanum contents (x = 1, 0.9) adopt cation-disordered $(La_{1-x}Ca_x)_{0.5}Mn_{0.5}O$ rocksalt structures. The transformation from a $La_{1-x}Ca_xMnO_3$ perovskite structure to a $(La_{1-x}Ca_x)_{0.5}Mn_{0.5}O$ rocksalt structure is a relatively low-energy process because the two structure types share a common cation lattice as shown in Figure 10a,b. Therefore low-temperature deintercalation of oxide ions and an associated rearrangement of the anion lattice can readily convert perovskite phases into cation-ordered rocksalt phases, as has been previously observed during the hydrogen reduction of $CaMnO_3$ to $Ca_{0.5}Mn_{0.5}O$.[25] We have not observed any explicit evidence for cation order in the $(La_{1-x}Ca_x)_{0.5}Mn_{0.5}O$ (x = 1, 0.9) phases prepared in this study, suggesting a further transformation to cation-disordered rocksalt phases has occurred on reduction with sodium hydride (Figure 10c). Similar disordered $Ca_{0.5}Mn_{0.5}O$ rocksalt phases can be prepared by sintering CaO and MnO at high temperature, indicating these are thermodynamically stable phases.[25,26]

In contrast to the calcium-rich $La_{1-x}Ca_xMnO_{2+\delta}$ phases, the lanthanum-rich reduced materials ($0.6 \leq x \leq 0.7$) adopt anion-deficient tetragonal structures which retain the ordered cation lattices of the parent perovskite phases. The anion deficiency in these tetragonal phases is accommodated within equatorial layers of composition MnO. These layers exist either as sheets of edge-sharing MnO_6 octahedra or sheets of corner-sharing MnO_4 tetrahedra as shown in Figure 3c,d, with the extended structure being constructed from a disordered stacking of these sheets. Analysis of the local structure of samples using RMC models, confirms this structural model and reveal significant 'relaxation' from the average structures refined against Bragg scattering. This is particularly apparent within the tetrahedral layers of the materials, which have longer and chemically more reasonable Mn—O bond

Table 3. Selected Bond Lengths (Å) from the Local, ⟨A−B⟩, and Average, ⟨A⟩−⟨B⟩, Structures of $La_{1-x}Ca_xMnO_{2+\delta}$ Phases

		tetrahedral			octahedral	
x	length	Mn−O(1) (ax)	Mn−O(3) (equiv)	O(3)−O(3)	Mn−O(1) (ax)	Mn−O(2) (equiv)
0.6	⟨A⟩−⟨B⟩	2.212(1)	1.816(1)	2.568(4)	2.212(1)	2.502(1)
	⟨A−B⟩	2.401(7)	2.115(3)	2.807(6)	2.214(2)	2.554(2)
0.67	⟨A⟩−⟨B⟩	2.227(1)	1.802(1)	2.594(3)	2.227(1)	2.480(1)
	⟨A−B⟩	2.390(5)	2.083(3)	2.739(7)	2.220(2)	2.525(2)
0.7	⟨A⟩−⟨B⟩	2.243(1)	1.791(1)	2.533(6)	2.243(1)	2.459(1)
	⟨A−B⟩	2.433(6)	2.076(3)	2.760(9)	2.250(3)	2.510(2)

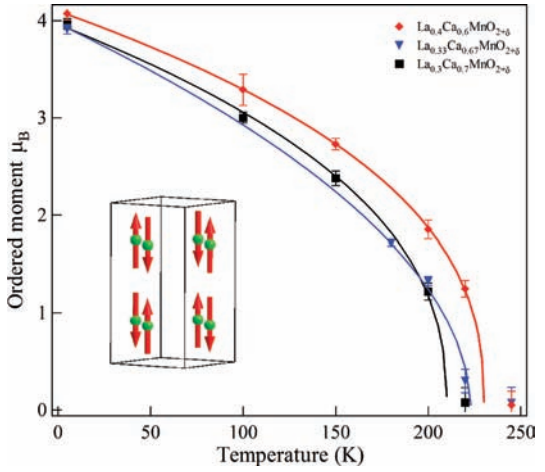

Figure 9. Plot of the refined ordered magnetic moment as a function of temperature for $La_{1-x}Ca_xMnO_{2+\delta}$ (x = 0.6, 0.67, 0.7) phases. Inset shows the antiferromagnetically ordered structure of the $La_{1-x}Ca_xMnO_{2+\delta}$ (x = 0.6, 0.67, 0.7) phases.

Table 4. Parameters Extracted from Structural and Magnetic Fits to Low-Temperature Neutron Powder Diffraction Data Collected from $La_{1-x}Ca_xMnO_{2+\delta}$ Phases

phase	$\mu_{observed}$ at 5 K (μ_B)	$\mu_{expected}$ (μ_B)	T_N (K)	β
$La_{0.4}Ca_{0.6}MnO_2$	4.07(6)	4.60	231	0.548
$La_{0.33}Ca_{0.67}MnO_2$	3.91(4)	4.67	221	0.508
$La_{0.3}Ca_{0.7}MnO_2$	3.96(5)	4.70	214	0.442

lengths and O−O separations within the local structure descriptions than in the average structures (Table 3). Given this degree of structural relaxation, it is unsurprising that the displacement ellipsoids refined for atoms within the average structure are so large (Table 2).

Comparison of Figures 3c and 10b reveals that the octahedral layers, which form part of the disordered structures of $La_{1-x}Ca_xMnO_{2+\delta}$ (x = 0.6. 0.67, 0.7) phases, correspond to slices through the rocksalt structure. Therefore the structures of the $La_{1-x}Ca_xMnO_{2+\delta}$ (x = 0.6. 0.67, 0.7) phases can be described as cation-ordered rocksalt lattices intergrown with 'defect' tetrahedral layers, the presence of which drive the average lattice symmetry from cubic to tetragonal. As the lanthanum concentration decreases (increasing x) across the $La_{1-x}Ca_xMnO_{2+\delta}$ compositional series there is a steady decrease in the concentration of

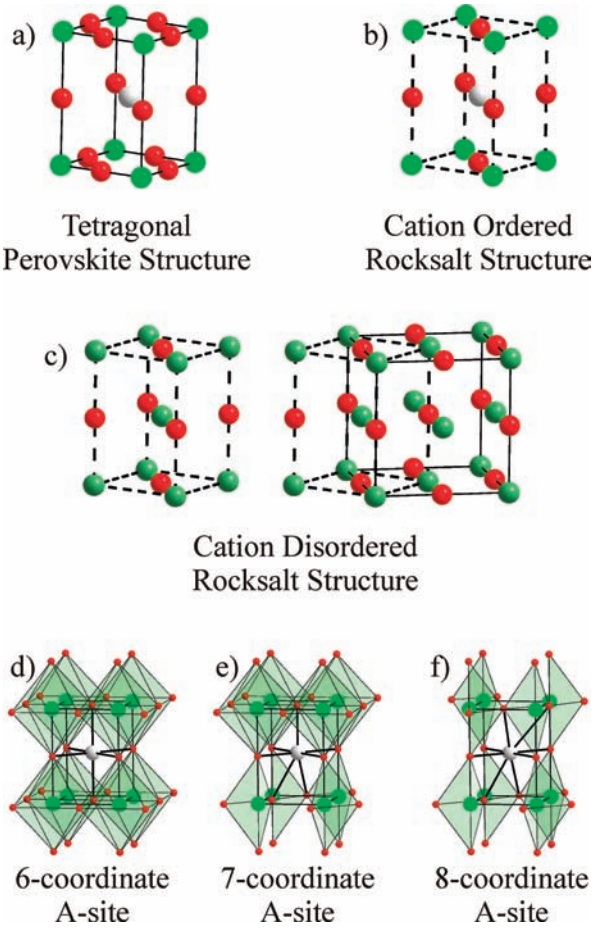

Figure 10. (a) Tetragonal perovskite structure, (b) the cation-ordered rocksalt structure (tetragonal unit cell) and (c) the cation-disordered rock salt structure (tetragonal and face-centered cubic unit cells). The (d) 6-coordinate (A-cation between two octahedral layers), (e) 7-coordinate (A-cation between one octahedral and one tetrahedral layer) and (f) 8-coordinate (A-cation between two tetrahedral layers) A-cation sites in the disordered structures of $La_{1-x}Ca_xMnO_{2+\delta}$ (x = 0.6, 0.67, 0.7) phases. In all parts of the figure oxide ions are red, manganese ions are green, and La/Ca cations are gray.

'defect' tetrahedral layers from 46% of layers at x = 0.6 to 33% of layers at x = 0.7. Associated with this decline in concentration there is a steady increase in the c/a ratio of lattice parameters (Table 1) which approaches the value of $\sqrt{2}$ expected for a face-centered cubic rocksalt lattice described in a tetragonal unit cell (Figure 10b). Furthermore the positions of atoms within octahedral

layers become more regular, as revealed by the RMC optimized structural models. Examination of X-ray powder diffraction data collected from $La_{0.2}Ca_{0.8}MnO_{2+\delta}$ (Figure 1) reveals that this phase not only has a composition that lies between the cubic and tetragonal $La_{1-x}Ca_xMnO_{2+\delta}$ phases but also appears to be a hybrid of the tetragonal structures observed for lanthanum-rich $La_{1-x}Ca_xMnO_{2+\delta}$ phases and the cubic structures observed for the calcium-rich $(La_{1-x}Ca_x)_{0.5}Mn_{0.5}O$ phases. All these observations are consistent with a continuous transformation, as a function of declining lanthanum concentration, from a set of phases which are disordered intergrowths of tetrahedral and octahedral layers to a set of nondefective rocksalt-type phases.

This structural progression as a function of La:Ca ratio can be rationalized by observing that despite the rather dissimilar 6-coordinate ionic radii of Mn^{2+} (r = 0.83 Å) and Ca^{2+} (r = 1.00 Å),[27] both metals form monoxides which adopt rocksalt structures. These two rocksalt phases have rather dissimilar lattice parameters (CaO, a = 4.812 Å; MnO, a = 4.444 Å) but nevertheless form a solid solution over the entire $Ca_{1-x}Mn_xO$ ($0 < x < 1$) compositional range.[26] Thus, it is not surprising that the reduction of the perovskite phase $CaMnO_3$ yields the rocksalt phase $Ca_{0.5}Mn_{0.5}O$.

The introduction of 'defect' tetrahedral layers into the rocksalt lattice raises the coordination number of the La/Ca A-cation sites from 6-coordinate (A-cation between two octahedral layers) to 7-coordinate (A-cation between one octahedral and one tetrahedral layer) or even 8-coordinate (A-cation between two tetrahedral layers) as shown in Figure 10d, e, and f, respectively. Although the 6-coordinate ionic radius of La^{3+} (r = 1.03 Å)[27] is rather similar to that of Ca^{2+}, lanthanum cations rarely occupy 6-coordinate sites and are normally observed with 7-fold coordination (e.g., La_2O_3) or higher.[28] Thus, the presence of 'defect' tetrahedral layers within the structures of $La_{1-x}Ca_xMnO_{2+\delta}$ (x = 0.6, 0.67, 0.7) phases can be attributed to the need to accommodate La^{3+} cations in sites of higher coordination number than Ca^{2+}.

XANES data collected from $La_{1-x}Ca_xMnO_{2+\delta}$ phases unambiguously reveal the presence of Mn(I) centers in all samples with $x < 1$. While monovalent manganese organometallic complexes are relatively well-known, particularly when π-acceptor ligands are used to stabilize the electron-rich metal centers, to our knowledge the $La_{1-x}Ca_xMnO_{2+\delta}$ phases described here are the first credible report of monovalent manganese centers in extended oxides.

With the exception of Cu(I) which is common, monovalent cations of the elements of the first transition series (Ti−Cu) are relatively rare in extended oxide phases as they are readily oxidized, even by species which would not normally be considered oxidizing agents. Low-temperature topotactic reduction reactions can be used to prepare oxide phases containing monovalent cations of metals late in the transition series, such as Ni(I)[12,13] and Co(I),[14,29] because the increase in the electronegativity of transition metals as the series progresses helps to stabilize the +1 oxidation state to some extent.[28] However, the phases produced by this route are still strong reducing agents. Alternatively, in the presence of highly electropositive elements, such as alkali metals, oxide phases such as $K_3M^IO_2$ (M = Fe, Co, Ni)[30,31] can be prepared which contain monovalent late transition metal centers—although it should be noted the transition metal centers in these phases reside within discrete $M^IO_2^{3-}$ linear anions, rather than an extended metal−oxygen lattice.

Manganese resides in the middle of the transition series and generally exhibits oxidation states between +2 and +7 in oxide phases,[28] consistent with this position. Therefore, the observation of Mn(I) centers in the $La_{1-x}Ca_xMnO_{2+\delta}$ phases suggests these materials are highly metastable. Insight into the kinetic stabilization of Mn(I) centers within $La_{1-x}Ca_xMnO_{2+\delta}$ phases can be gained by considering the reduction reactions of other transition metal perovskite phases. If the perovskite phases $LaCoO_3$ or $LaNiO_3$ are heated to 800 °C in hydrogen, they decompose by expelling La_2O_3 and forming elemental cobalt or nickel.[32,33] In contrast if $LaMnO_3$ is heated under the same conditions, it decomposes to La_2O_3 and MnO,[34] emphasizing the thermodynamic stability of this rock salt phase and its resistance to chemical reduction. We propose that it is this stability and that of the related $Ca_{1-x}Mn_xO$ rocksalt phases which stabilize the Mn(I)-containing $La_{1-x}Ca_xMnO_{2+\delta}$ materials.

Sodium hydride acts as a powerful reducing agent at low temperature, rapidly reducing $CaMnO_3$ to the Mn(II) phase $Ca_{0.5}Mn_{0.5}O$, rather than the Mn(III) phase $CaMnO_{2.5}$ prepared by low-temperature hydrogen reduction.[35] As described above, the transformation from $CaMnO_3$ perovskite to $Ca_{0.5}Mn_{0.5}O$ rocksalt is kinetically facilitated by the common cation lattice shared by the two structures (Figure 10a and b); thus, no long-range cation diffusion is required during the transformation, and the reaction is driven by the thermodynamic stability of the rocksalt phase which is formed.[25,26] Reduction of the analogous $La_{1-x}Ca_xMnO_3$ perovskite phases follows a similar path to form materials with structures based on that of rocksalt. However, as the reduction reactions are performed at low temperature, there is insufficient energy to expel the lanthanum cations from the ternary oxide phase and form mixtures of $Ca_{0.5-x}Mn_{0.5+x}O$ and $^x/_2La_2O_3$ in reactions analogous to the decomposition of $LaMnO_3$. Thus, the lanthanum cations are incorporated within the rocksalt lattice. However, the rocksalt lattice cannot readily accommodate excess oxygen without incurring significant energetic penalties, and therefore, Mn(II) phases of composition $La_{1-x}Ca_xMnO_{2+(1-x)/2}$ are strongly disfavored, and the observed $La_{1-x}Ca_xMnO_{2+\delta}$ Mn(I) phases are formed. The only structural modification made to accommodate the lanthanum within the rocksalt lattice is the presence of defect tetrahedral layers described above. However these layers cannot accommodate 'extra' oxygen due to the contraction in the *ab*-plane on reduction. Thus, it can be seen that the Mn(I) centers observed in $La_{1-x}Ca_xMnO_{2+\delta}$ phases are stabilized by the high thermodynamic stability of the $Ca_{1-x}Mn_xO$ framework in which they reside.

There is no evidence for Mn(I)/Mn(II) charge order within the reduced materials. There is a correlation between the number of defect tetrahedral layers in $La_{1-x}Ca_xMnO_{2+\delta}$ phases and the concentration of Mn(I) cations; however, bond valence sums calculated for the different manganese coordination sites in the reduced phases (Table 5) provide no evidence for the localization of monovalent manganese cations on tetrahedral coordination sites.

Table 5. Bond Valence Sums Calculated for the Manganese Coordination Sites within $La_{1-x}Ca_xMnO_{2+\delta}$ Phases

	octahedral site BVS	tetrahedral site BVS
$La_{0.4}Ca_{0.6}MnO_{2+\delta}$	1.14	1.21
$La_{0.33}Ca_{0.67}MnO_{2+\delta}$	1.17	1.30
$La_{0.3}Ca_{0.7}MnO_{2+\delta}$	1.14	1.27
$(La_{0.1}Ca_{0.9})_{0.5}Mn_{0.5}O$	1.39	
$Ca_{0.5}Mn_{0.5}O$	1.47	

$La_{0.4}Ca_{0.6}MnO_{2+\delta}$, $La_{0.33}Ca_{0.67}MnO_{2+\delta}$, and $La_{0.3}Ca_{0.7}MnO_{2+\delta}$ all exhibit G-type antiferromagnetic order (Figure 9), with ordering temperatures in the range 214−231 K and ordered moments at 5 K, corresponding to between 84% and 88% of those expected for mixtures of $s = {}^5/_2$ Mn(II) and $s = 2$ Mn(I) centers. This behavior is consistent with strong σ-type antiferromagnetic exchange interactions.

In conclusion, the low-temperature reduction of $La_{1-x}Ca_xMnO_3$ ($0.6 < x < 1$) perovskite phases with sodium hydride allows the preparation of the corresponding $La_{1-x}Ca_xMnO_{2+\delta}$ phases and the stabilization of Mn(I) centers in an extended oxide framework.

■ ASSOCIATED CONTENT

Supporting Information. Refined structures of $Ca_{0.5}Mn_{0.5}O$ and $(La_{0.1}Ca_{0.9})_{0.5}Mn_{0.5}O$. Description of the four different tetrahedral layers used in the local-structure refinements. List of the minimum atomic separations allowed in the local-structure refinements. Observed, calculated, and difference plots from the structural and magnetic refinements performed against neutron powder diffraction data collected from $La_{1-x}Ca_xMnO_{2+\delta}$ ($x = 0.6$, 0.67, 0.7) at 5 K. This material is available free of charge via the Internet at http://pubs.acs.org.

■ AUTHOR INFORMATION

Corresponding Author
michael.hayward@chem.ox.ac.uk

■ ACKNOWLEDGMENT

We thank R. Smith and E. Suard for assistance collecting the neutron diffraction data. Experiments at the ISIS pulsed neutron facility were supported by a beam time allocation from the Science and Technology Facilities Council. Electron diffraction experiments were made with financial support from the European Union under the Framework 6 program under a contract for an Integrated Infrastructure Initiative, Reference 026019 ESTEEM. E.D. thanks the EPSRC for a studentship. A.L.G. thanks EPSRC for support under Grant EP/G 004528/2.

■ REFERENCES

(1) Bednorz, J. G.; Muller, K. A. *Z. Phys. B* **1986**, *64*, 189–193.
(2) Rao, C. N. R.; Raveau, B., Eds. *Colossal Magnetoresistance, Charge Ordering and Related Properties of Manganese Oxides*; World Scientific: Singapore, 1998.
(3) Lines, M. E.; Glass, A. M. *Principles and Applications of Ferroelectrics and Related Materials*; Oxford University Press: Oxford, 1991.
(4) Cooper, S. L.; Egami, T.; Goodenough, J. B.; Zhou, J.-S. *Localized to Itinerant Electronic Transition in Perovskite Oxides*; Springer-Velang: Berlin, Heidelburg, New York, 2001.
(5) Tarascon, J. M.; Armand, M. *Nature* **2001**, *414*, 359–367.
(6) Reaney, I. M.; Iddles, D. *J. Am. Ceram. Soc.* **2006**, *89*, 2063–2072.
(7) Pena, M. A.; Fierro, J. L. G. *Chem. Rev.* **2001**, *101*, 1981–2017.
(8) Goodenough, J. B.; Zhou, J.-S. *Chem. Mater.* **1998**, *10*, 2980–2993.
(9) Schaak, R. E.; Mallouk, T. E. *Chem. Mater.* **2002**, *14*, 1455–1471.
(10) Ranmohotti, K. G. S.; Josepha, E.; Choi, J.; Zhang, J. X.; Wiley, J. B. *Adv. Mater.* **2011**, *23*, 442–460.
(11) Gopalakrishnan, J. *Chem. Mater.* **1995**, *7*, 1265–1275.
(12) Hayward, M. A.; Green, M. A.; Rosseinsky, M. J.; Sloan, J. *J. Am. Chem. Soc.* **1999**, *121*, 8843–8854.
(13) Poltavets, V. V.; Lokshin, K. A.; Dikmen, S.; Croft, M.; Egami, T.; Greenblatt, M. *J. Am. Chem. Soc.* **2006**, *128*, 9050–9051.
(14) Seddon, J.; Suard, E.; Hayward, M. A. *J. Am. Chem. Soc.* **2010**, *132*, 2802–2810.
(15) Tsujimoto, Y.; Tassel, C.; Hayashi, N.; Watanabe, T.; Kageyama, H.; Yoshimura, K.; Takano, M.; Ceretti, M.; Ritter, C.; Paulus, W. *Nature* **2007**, *450*, 1062–1065.
(16) Dixon, E.; Hayward, M. A. *Inorg. Chem.* **2010**, *49*, 9649–9654.
(17) Casey, P. S.; Barker, D.; Hayward, M. A. *J. Solid State Chem.* **2006**, *179*, 1375–1382.
(18) Parsons, T. G.; D'Hondt, H.; Hadermann, J.; Hayward, M. A. *Chem. Mater.* **2009**, *21*, 5527–5538.
(19) Dixon, E.; Hadermann, J.; Hayward, M. A. *J. Solid State Chem.* **2011**, *184*, 1791–1799.
(20) Pissas, M.; Kallias, G. *Phys. Rev. B* **2003**, *68*, 134414.
(21) Poeppelmeier, K. R.; Leonowicz, M. E.; Scanlon, J. C.; Longo, J. M.; Yelon, W. B. *J. Solid State Chem.* **1982**, *45*, 71–79.
(22) Larson, A. C.; Von Dreele, R. B. General Structure Analysis System (GSAS). *Los Alamos National Laboratory Report, LAUR 86-748*; 2000.
(23) Keen, D. A. *J. Appl. Crystallogr.* **2001**, *34*, 172–177.
(24) Tucker, M. G.; Keen, D. A.; Dove, M. T.; Goodwin, A. L.; Hui, Q. *J. Phys.: Condens. Matter* **2007**, *19*, 335218.
(25) Varela, A.; de Dios, S.; Parras, M.; Hernando, M.; Fernandez-Diaz, M. T.; Landa-Canovas, A. R.; Gonzalez-Calbet, J. M. *J. Am. Chem. Soc.* **2009**, *131*, 8660–8668.
(26) Sagdeo, P. R.; Shahid, A.; Lalla, N. P. *Powder Diffraction* **2006**, *21*, 40–44.
(27) Shannon, R. D. *Acta Crystallogr.* **1976**, *A32*, 751–767.
(28) Greenwood, N. N.; Earnshaw, A. *Chemistry of the Elements*; Pergamon Press: Oxford, 1997.
(29) Hayward, M. A.; Rosseinsky, M. J. *Chem. Mater.* **2000**, *12*, 2182–2195.
(30) Bernhardt, F.; Hoppe, R. *Z. Anorg. Allg. Chem.* **1993**, *619*, 969–975.
(31) Byeon, S. H.; Kim, H. J.; Kim, D. K.; Hur, N. H. *Chem. Mater.* **2003**, *15*, 383–389.
(32) Ivanova, S.; Senyshyn, A.; Zhecheva, E.; Tenchev, K.; Nikolov, V.; Stoyanova, R.; Fuess, H. *J. Alloys Compd.* **2009**, *480*, 279–285.
(33) Martinezlope, M. J.; Alonso, J. A. *Eur. J. Solid State Inorg. Chem.* **1995**, *32*, 361–371.
(34) Kuo, J. H.; Anderson, H. U.; Sparlin, D. M. *J. Solid State Chem.* **1989**, *83*, 52–60.
(35) Poeppelmeier, K. R.; Leonowicz, M. E.; Longo, J. M. *J. Solid State Chem.* **1982**, *44*, 89–98.